

Full length article

A non-Schmid crystal plasticity finite element approach to multi-scale modeling of nickel-based superalloys



Shahriyar Keshavarz^{a, b, *}, Somnath Ghosh^{c, d, e}, Andrew C.E. Reid^b, Stephen A. Langer^b

^a Theiss Research, 7411 Eads Ave, La Jolla, CA 92037, United States

^b National Institute of Standards and Technology, 100 Bureau Dr, Gaithersburg, MD 20899, United States

^c Department of Civil Engineering, Johns Hopkins University, Baltimore, MD 21218, United States

^d Department of Mechanical Engineering, Johns Hopkins University, Baltimore, MD 21218, United States

^e Department of Materials Science & Engineering, Johns Hopkins University, Baltimore, MD 21218, United States

ARTICLE INFO

Article history:

Received 23 February 2016

Received in revised form

3 May 2016

Accepted 8 May 2016

Available online 21 May 2016

Keywords:

Ni-based superalloys

Homogenization

Crystal plasticity

Morphology

Non-Schmid

ABSTRACT

This paper develops non-Schmid crystal plasticity constitutive models at two length scales, and bridges them in a multi-scale framework. The constitutive models address thermo-mechanical behavior of Nickel-based superalloys for a large temperature range, viz. 300 K–1223 K, and include orientation dependencies and tension-compression asymmetry. The orientation dependencies result in tension-compression asymmetry for almost all orientations on the standard unit triangle. However simulations show different trends for the stronger direction (tension or compression) in terms of yield stress and hardening. The multi-scale framework includes two sub-grain and homogenized grain scales. For the sub-grain scale, a size-dependent, dislocation density-based FEM model of the representative volume element (RVE) with explicit depiction of the γ - γ' morphology is developed as a building block for homogenization. For the next scale, an activation energy based crystal plasticity (AE-CP) model is developed for single crystal Ni-based superalloys. The homogenized AE-CP model develops functional forms of constitutive parameters in terms of characteristics of the sub-grain γ - γ' microstructural morphology including γ' shape, volume fraction and γ channel-width in the sub-grain microstructure. This homogenized model can significantly expedite crystal plasticity FE simulations due to the parametrized representation, while retaining accuracy.

© 2016 Acta Materialia Inc. Published by Elsevier Ltd. All rights reserved.

1. Introduction

Nickel based superalloys are used extensively in the aero-engine industry for turbine blades and disks in the form of single crystals and polycrystals. These alloys contain multiple phases including regular FCC crystal structure mainly Ni in γ channel and $L1_2$ ordered crystal structure in γ' precipitates as indicated in Fig. 1. The $L1_2$ crystal structure is derived from an FCC lattice, for which a simple cubic sub-lattice is occupied by minority atoms and the three additional sub-lattices are occupied by majority atoms [1]. The ordered structure γ' phase is a strengthening constituent with special thermo-mechanical properties to the overall superalloy and depends on the heat treatment. γ' precipitates in Nickel-based

superalloys has Ni_3Al -based compositions with $L1_2$ crystal structure where the corner sites are occupied by the minority (Al) atoms and the face-centered sites are occupied by the majority (Ni) atoms. The major micro-mechanical difference between these two phases is super-dislocation mechanism in Ni_3Al compounds instead of regular dislocation in FCC crystal structure with almost twice the size of Burgers vector.

The morphology of precipitates including shape, size and volume fraction depend largely on the cooling rate [3,4] as well as on the internal stress-gradients [5] encountered during casting and heat treatment processes. The average size of γ' precipitates, their shape, and volume fraction have a major impact on their mechanical responses [6,7].

Mechanical properties, including dislocation mechanisms have been studied extensively for both single and polycrystals of these alloys in Ref. [8]. At lower temperatures, octahedral slip systems are mainly active and slip occurs on these slip systems in both phases. As temperature increases dislocations in intermetallic γ' phase,

* Corresponding author. Theiss Research, 7411 Eads Ave, La Jolla, CA 92037, United States.

E-mail address: shahriyar.keshavarzhadad@nist.gov (S. Keshavarz).

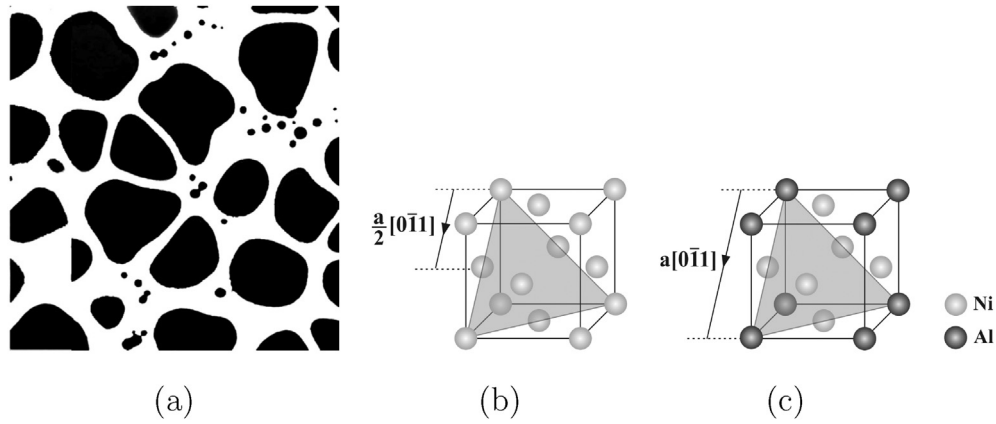


Fig. 1. Two-phase Nickel-based superalloys: (a) morphology of Rene 88-DT [2] including γ channel (the white area) and γ' particles (the dark area), (b) crystalline structure of γ phase, and (c) crystalline structure of γ' phase.

which are mostly screw dislocations, tend to be locked in a Kear-Wilford (KW) configuration due to cross-slip [9]. The rate of lock formation increases as temperature rises to a maximum around 1000 K. The cross-slip and lock formation mechanisms are shown in Fig. 2. The mechanisms need not only consider the activation of octahedral slip systems but also the activation of cube slip systems. The activation of cube slip systems is more pronounced for

temperatures above the temperature of peak cross-slip rate or critical temperature, which is around 1000 K. However, above this temperature, edge and screw dislocations on cube planes happen without any cross-slip. In order to include cross-slip mechanism into the crystal plasticity constitutive model, the enthalpy term suggested in Ref. [10] is considered. The term includes non-Schmid components of the shear stress as shown in Fig. 2 rather than the

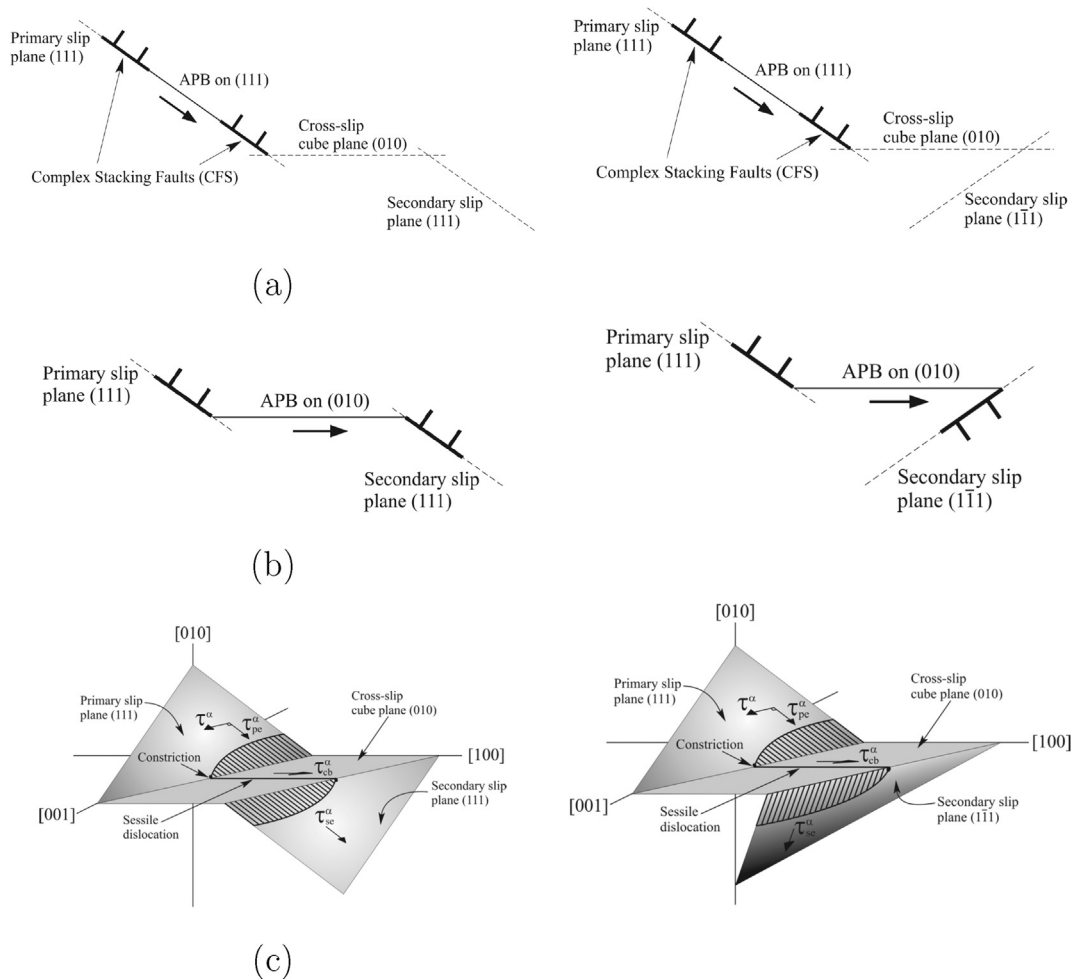


Fig. 2. Kear-Wilford lock formation: (a) formation of anti-phase boundary, (b) possible anti-phase boundary configurations, and (c) 3D configuration of Kear-Wilford lock.

resolved shear stress or Schmid components. The same mechanism is considered in Ref. [11] to determine the slip system resistance due to cross-slip pinning. The aim of the present study is to develop a morphology dependent constitutive model incorporating non-Schmid shear stresses and APB shearing that can capture the temperature dependency of yield stress, strain hardening and creep behavior of Nickel-based superalloys. This constitutive model can manifest tension-compression asymmetry for different crystal orientations.

Modeling of Ni-based superalloys needs not only to incorporate small length scale microstructural mechanisms e.g. dislocation activities, but must also establish links with higher scales to simulate polycrystalline microstructures [6,12,13]. From a computational point of view, it is prohibitive to model polycrystalline superalloy microstructures with explicit representation of the γ - γ' microstructures. Multi-scale schemes should be applied in order to bridge between scales [14–16]. The parametric forms and their evolution of constitutive models can accurately represent the effect of microstructural morphology and deformation mechanisms. Therefore, polycrystalline model of Ni-based superalloys can be governed by features at three dominant scales, viz. (1) the sub-grain single crystal scale: including the morphology of the γ phase containing the size of them or γ channel-width, (2) the single crystal homogenized grain-scale: including parametric constitutive equations, and (3) the polycrystalline grain-scale: including grain boundaries and crystal orientations as shown in Fig. 3. The sub-grain scale study includes investigation of dislocation

mechanisms through a non-Schmid constitutive model which depends on the critical microstructural and mechanical features in plasticity models. The microstructural features incorporate morphology and crystallography of the materials while the mechanical features include load intensity, load rate, and temperature. The next step focuses on the homogenized single crystal grain-scale model where a homogenized non-Schmid constitutive model is developed incorporating morphology-based variables. The homogenized model incorporates temperature variation from room temperature to 1223 K, orientation dependencies to capture asymmetry in tension and compression. The resulting hierarchical model has the potential of significantly expediting single crystal simulations, while retaining accuracy. Section 2 introduces the two-phase sub-grain scale with a non-Schmid constitutive model in the crystal plasticity framework. The homogenized single crystal model for the next scale begins in Section 3 to develop a homogenized non-Schmid constitutive model. The homogenization procedure that yields morphology-dependent constitutive parameters and their calibration and validation with sub-grain RVE models as well as experimental results, are discussed in Section 4. A summary in Section 5 concludes the paper.

While this work provides a stand-alone solution to the multi-scale CPFEM problem it addresses, the model and techniques developed here are also intended to be incorporated into the Object-Oriented Finite Element code, or OOF [17]. It is a general-purpose modeling code intended to assist materials scientists and materials engineers in undertaking computational investigations of

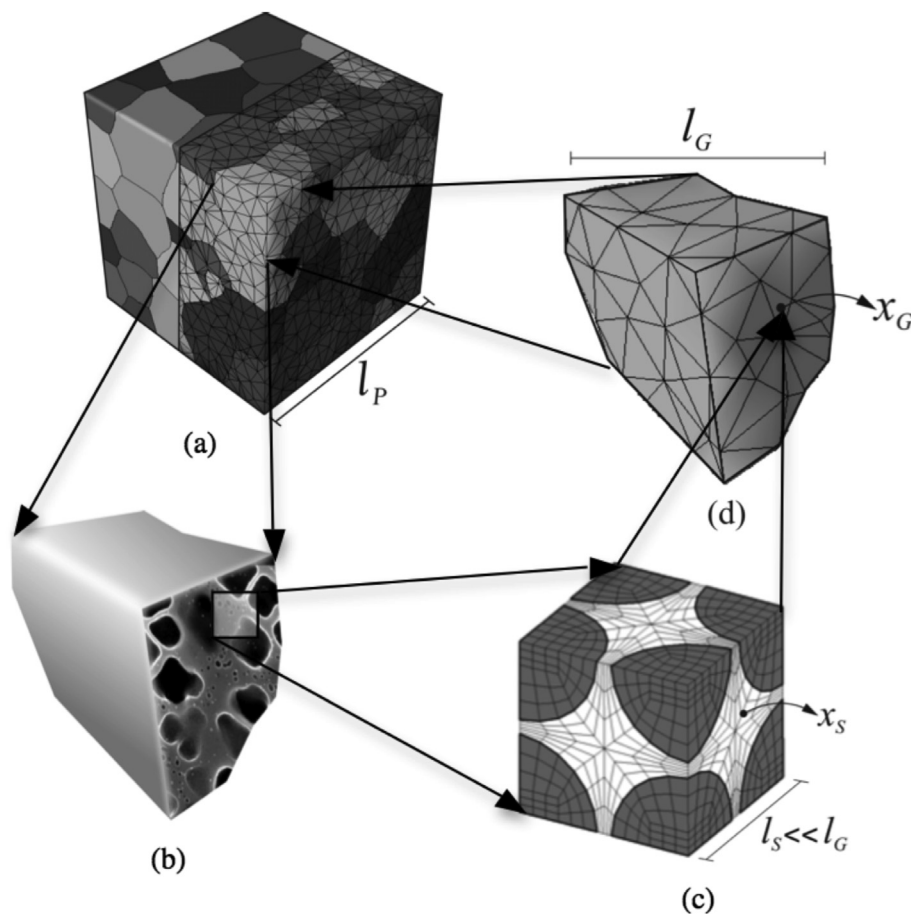


Fig. 3. Schematic representation of three scales for Ni-based superalloys in the crystal plasticity finite element framework: (a) polycrystalline microstructure showing the grains and CPFEM mesh, (b) single grain description of a two-phase material, (c) discretized sub-grain scale two-phase microstructure, and (d) homogenized single crystal grain-scale finite element model.

structure–property relations in a large variety of systems, including mechanical systems whose behavior is dominated by crystal plasticity.

2. Two-phase γ - γ' sub-grain scale of nickel superalloys

The material studied is a two-phase, binary Nickel-based superalloy consisting of γ (Ni) and γ' (Ni₃Al) phases. Plastic deformation is accumulated through crystallographic slip on activated slip systems, which is different in the two phases. These contribute to plastic anisotropy of the sub-grain microstructure. A dislocation density constitutive model, proposed in Refs. [6], is modified for a large temperature range (300 K < T < 1223 K). It should be noted that rafting occurs when single crystal superalloys are subjected to stress at elevated temperature (T > 900 °C), which is not considered in this study. The model counts for all crystal orientations in tension and compression and employed to simulate the rate-dependent plastic behavior. It incorporates evolution of statistically stored dislocations (SSDs) in both phases due to various dislocation mechanisms, annihilation and generation, while cross-slip dislocations (CSDs) are considered just for γ' phase. In order to take into account the gradient of plastic strain at the geometrically incompatible locations such as matrix-precipitate interface and grain boundaries, geometrically necessary dislocations (GNDs) are incorporated.

Deformation of Nickel-based superalloys includes the activation of 12 octahedral slip systems and 6 cube slip systems. However the dislocation mechanisms are different in γ -channel and in precipitates. The length of a full dislocation or super-dislocation in precipitates dominant with Ni₃Al + XX compositions is $\langle 110 \rangle$, almost twice as a full dislocation in regular FCC crystals which is $\frac{1}{2}\langle 110 \rangle$. This long Burgers vector results in complicated dislocation mechanisms. The dominant mechanism in precipitates for almost all ranges of temperatures is the dissociation of a screw super-dislocation into two super-partials, which have a Burgers vector of $\frac{1}{2}\langle 1\bar{1}0 \rangle$. These create a planar fault anti-phase boundary or APB. Afterward, these super-partials basically split into two Shockley partials, to bound a complex stacking fault (CSF) with Burgers vectors of $\frac{1}{6}\langle 11\bar{2} \rangle$ as shown in Fig. 2. According to this figure, three non-Schmid shear stresses τ_{pe}^α , τ_{cb}^α and τ_{se}^α acting on primary octahedral, cube and secondary octahedral slip planes respectively are considered in the thermally activated cross-slip mechanism [18], where these long screw dislocations tend to be primarily locked in the KW configurations with increasing in temperature. Therefore, $\{111\}\langle\bar{1}01\rangle$ screw super-dislocations are able to cross-slip from an octahedral slip plane onto a cube slip plane due to a drop in the APB energy. Hence, the dislocation gets locked because it is not energy favor for the dislocation to move forward on the octahedral planes any more. This mechanism in Ni₃Al + XX compositions do not follow the Schmid's law in most materials [19] according to experimental observations. Materials which follow Schmid's law usually have symmetric evolution for hardness while the evolution of hardness of the immobile cross-slip dislocations are not symmetric and changes with crystal orientations and even it is different in compression and tension for a given orientation. For one of tensile or compressive loads, τ_{pe}^α constricts the Shockley partials to increase cross-slip rates which results in a promotion of the yield stress. For reversed loading direction, it hinders cross-slip with a demotion in the yield stress. Therefore, beside twelve octahedral slip systems, six cube slip systems with three planes of the $\{001\}$ family, each with two slip directions $\langle 01\bar{1} \rangle$ can be activated to incorporate the cube shear stresses (τ_{cb}^α).

2.1. Dislocation density-based constitutive model

The crystal plasticity constitutive model divides the deformation gradient \mathbf{F} into an elastic part \mathbf{F}^e for elastic stretching and rigid-body rotations and a plastic part \mathbf{F}^p without volume change associated with just slip in the absence of rotation in a multiplicative form of $\mathbf{F} = \mathbf{F}^e \mathbf{F}^p$. Velocity gradient associated with the plastic part \mathbf{L}^p can be calculated as a function of the rate of plastic shear strain $\dot{\gamma}^\alpha$ on all slip systems as

$$\mathbf{L}^p = \dot{\mathbf{F}}^p \mathbf{F}^{-p} = \sum_{\alpha=1}^N \dot{\gamma}^\alpha \mathbf{s}_0^\alpha = \sum_{\alpha=1}^N \dot{\gamma}^\alpha \mathbf{m}_0^\alpha \otimes \mathbf{n}_0^\alpha \quad (1)$$

where $\mathbf{s}_0^\alpha = \mathbf{m}_0^\alpha \otimes \mathbf{n}_0^\alpha$ is the Schmid tensor for the slip direction \mathbf{m}_0^α and slip plane normal \mathbf{n}_0^α in the reference configuration. The evolution of the deformation gradient associated with the plastic part $\dot{\mathbf{F}}^p$ can be calculated from this equation. An integration scheme is used to integrate $\dot{\mathbf{F}}^p$ in order to calculate the total plastic part of the deformation gradient then using the multiplicative form can result in the elastic part of the deformation. The Green-Lagrange strain tensor and the second Piola-Kirchhoff stress are calculated in the intermediate configuration as:

$$\mathbf{S} = \det(\mathbf{F}^e) \mathbf{F}^{e-1} \boldsymbol{\sigma} \mathbf{F}^{e-T} = \mathbf{C} : \mathbf{E}^e \text{ and } \mathbf{E}^e = \frac{1}{2} (\mathbf{F}^{eT} \mathbf{F}^e - \mathbf{I}) \quad (2)$$

where $\boldsymbol{\sigma}$ is the Cauchy stress tensor, \mathbf{C} is the anisotropic elasticity tensor which is a fourth order tensor and, \mathbf{I} is the identity tensor.

The plastic shear strain rate on a slip system is given by the Orowan equation as $\dot{\gamma}^\alpha = \rho_M^\alpha b^\alpha v^\alpha$ with the mobile dislocation density as ρ_M^α , Burgers vector as b^α and the dislocation velocity as v^α for a given slip system. The crystal plasticity framework incorporating the signed dislocation density used for superalloys in Ref. [6] is modified in the current study for rate-dependent plastic behavior. The modifications include adding cross-slip dislocation densities, temperature dependency of cross-slip shear resistance and considering cube slip systems in addition to octahedral slip systems. In general, the velocity of dislocations can be written as:

$$v^\alpha = v_0 \exp\left(-\frac{Q}{K_B \theta}\right) \sinh\left(\frac{|\tau^\alpha| - \tau_{pass}^\alpha}{\tau_{cut}^\alpha}\right)^p \text{sign}(\tau^\alpha) \quad (3)$$

The initial dislocation velocity is considered as $v_0 = \lambda_\alpha f_0$ where f_0 is the attack frequency and λ_α is a temperature dependent jump width. The jump width λ_α can be calculated in terms of parallel and

forest dislocation densities as $\lambda_\alpha = \frac{c_0}{\sqrt{\rho_p^\alpha \rho_f^\alpha}} \left(\frac{\theta}{\theta_{ref}}\right)^{c_1}$. The temperature

dependent velocity in this equation includes the absolute temperature θ and the activation energy Q . The exponent p in the \sinh term is changed for different hardening evolution. The dislocation velocity in this equation changes with the resolved shear stress due to the applied stress τ^α , the passing stress τ_{pass}^α parallel to the slip system and the cutting stress τ_{cut}^α perpendicular to the slip system. The slip system dependent hardening parameters are given as [20]:

$$\tau_{pass}^\alpha = c_2 G b \sqrt{\rho_p^\alpha + \rho_M^\alpha}, \quad \tau_{cut}^\alpha = \frac{c_3 K_B \theta}{b^2} \sqrt{\rho_f^\alpha} \quad (4)$$

where G is the shear modulus and c_2 and c_3 are material constants. Contributions to the total slip resistance are considered to be due to statistically stored dislocations or SSDs. Statistically stored dislocations ρ_{SSD}^α are rate dependent scalar dislocations, incorporating dislocation generation due to lock and dipole formation and

dislocation annihilation due to athermal and thermal processes given in Ref. [20].

Another part contributing in slip systems resistance is geometrically necessary dislocations (GNDs) which reflect the source of hardening due to inhomogeneity in superalloys. GNDs can be decomposed into three components including two edge parts and one screw part which are derived from the material time derivative of the Nye dislocation tensor [20]. The parallel and forest dislocation densities can be written as functions of SSDs and GNDs. Finally, the mobile dislocation density ρ_m^α is written as [18]:

$$\rho_M^\alpha = \frac{c_4 K_B \theta \sqrt{\rho_F^\alpha \rho_P^\alpha}}{G b^3} \quad (5)$$

where c_4 can be evaluated in terms of c_2 and c_3 as $c_4 = \frac{2c_3}{c_2}$.

2.2. Criteria for nucleation of dislocations in the precipitates (γ' phase)

The most dominant dislocation mechanism for all temperature ranges is dissociation of a super-dislocation into two partials separated by an anti-phase boundary or APB. These long screw dislocations incline to be locked in KW configurations and create local obstacles as temperature increases. The creation rate of these obstacles is a function of cross-slip rate which increases by increasing temperature. The enthalpy term for cross-slip changes as the non-Schmid shear stresses τ_{pe}^α , τ_{se}^α and τ_{cb}^α change. These components are responsible for dislocation dissociation during cross-slip mechanism however, there are no dislocation core effects for cube slip systems. Hence the dislocation nucleation criterion in γ' phase can be divided into two categories, viz. (1) for octahedral slip systems with non-Schmid effects and (2) for cube slip systems without non-Schmid effects. To accommodate these two conditions in the crystal plasticity constitutive models, the APB shearing criterion in Ref. [6] is extended as follows:

$$\tau_{eff}^\alpha = \left| \tau^\alpha \right| - \tau_{pass}^\alpha > \tau_c \quad (6)$$

where

$$\tau_{eff}^\alpha = \begin{cases} \left| \tau^\alpha \right| - \tau_{pass}^\alpha & \text{for } \left| \tau^\alpha \right| > \tau_{pass}^\alpha \\ 0 & \text{for } \left| \tau^\alpha \right| \leq \tau_{pass}^\alpha \end{cases} \quad (7)$$

This criterion is valid for both octahedral and cube slip systems. However the criterion for octahedral slip systems depends on the non-Schmid components, which means it changes as the crystal orientations change while for cube slip systems it is similar for all crystal orientations. Therefore, the critical shear in Eq. (6) system can be written as:

$$\tau_c^\alpha = \begin{cases} \tau_{co}^\alpha = \tau_{co}^\alpha(\tau_{pe}^\alpha, \tau_{se}^\alpha, \tau_{cb}^\alpha, \theta, \Gamma_{111}, \Gamma_{010}) & \text{on octahedral slip systems} \\ \tau_{cc} = \tau_{cc}(\theta) & \text{on cube slip systems} \end{cases} \quad (8)$$

For octahedral slip systems, the critical shear stress τ_{co}^α depends on the cross-slip dislocation density and can be expressed as

$$\tau_{co}^\alpha = \xi G \sqrt{\rho_{CSD}^\alpha} \quad (9)$$

Here G is the shear modulus [11]. The strength of the pinning obstacles can be accounted by the temperature parameter ξ . This strength decays exponentially when temperature increases, according to the following relation:

$$\xi = \xi_0 \exp\left(\frac{A}{\theta - \theta_c}\right) \quad (10)$$

There are three materials parameters ξ_0 , A and θ_c in this equation. θ_c is a critical temperature, which can be approximated as the precipitation temperature for γ' particles [11] and θ is the absolute temperature. The cross-slip dislocation density ρ_{CSD}^α can be stated as:

$$\rho_{CSD}^\alpha = \rho_0 \exp\left(-\frac{H^\alpha}{K_B \theta}\right) \quad (11)$$

The initial dislocation density ρ_0 is the cross-slip dislocation density at complete yield and H^α is the activation enthalpy term for cross-slip [18]:

$$H^\alpha = c_H \left\{ h + k_1 \left(t_{pe}^\alpha - k_2 t_{se}^\alpha \right) + \sqrt{\left(\frac{1}{\sqrt{3}} - \frac{\Gamma^{010}}{\Gamma^{111}} + \left| t_{cb}^\alpha \right| \right) \frac{b}{B}} \right\} \quad (12)$$

where h, k_1 and k_2 are materials constants to be calibrated, Γ^{111} and Γ^{010} (J/m²) are the APB energies per unit area on octahedral and cube planes respectively. t_{xx}^α is the normalized non-Schmid component of the resolved shear stress as $t_{xx}^\alpha = \frac{\tau_{xx}^\alpha}{\Gamma^{111}/b}$, $B = \frac{G b^2}{2\pi \Gamma^{111}}$ and $c_H = \frac{G b^3}{4\pi}$.

There are two important factors in increasing dislocation densities of the cross-slip mechanism, which are the creation of thermally activated constrictions and increasing temperature. The critical shear stress stated in Eq. (9) evolves by increasing dislocation densities of the cross-slip mechanism. However, the strength of obstacles decreases by an increase in the temperature according to Eq. (10). Hence, there is a competition between the increasing strength with formation of KW locks, and decreasing obstacle strength with increasing temperature.

2.3. Calibration of parameters in the constitutive law

There are two types of material constants in Eqs. (3)–(12). Constants in the first type can be found in the literature [21,11]. They include $h, \Gamma^{010}, \Gamma^{111}, b, G$ and ρ_0 , which have values 0.3, 0.083, 0.3, 2.49×10^{-10} m, 142.2 GPa, and 5.0×10^{15} m/m³ respectively. The statistically stored dislocation needs proper initial

values which is calibrated based on the experiments performed by Ref. [11] and can be stated as a function of temperature:

Table 1

Calibrated material constants for the constitutive model based on experimental data.

Parameter	p_{oct}	p_{cub}	$Q(J)$	k_1	k_2	ξ_0	A
Value	1.1	1.2	1.1×10^{-20}	0.5	0.6	1.8	325
Parameter	θ_c	θ_{ref}	$f_0(1/s)$	$c_0(1/m)$	c_1	c_2	c_3
Value	1400	300	10^8	0.078	-3.77	4	0.3

$$\rho_{SSDO} = \begin{cases} 4.04 \times 10^{11} - 3.34 \times 10^8 \theta & \theta \leq 659K \\ 2.42 \times 10^{11} - 0.87 \times 10^8 \theta & 659K < \theta \leq 930K \\ 13.28 \times 10^{11} - 12.58 \times 10^8 \theta & 930K < \theta \leq 1000K \\ 1.53 \times 10^{11} - 0.8 \times 10^8 \theta & \theta > 1000K \end{cases}$$

By using data given in Refs. [11], the cube slip resistance can be calibrated as a function of temperature as:

$$\tau_{cc} = \begin{cases} 460MPa & \theta \leq 915K \\ 1558 - 1.2\theta MPa & otherwise \end{cases}$$

The elastic stiffness tensor $\mathbf{C}_{\alpha\beta} = \mathbf{C}_{\beta\alpha}$ ($\alpha = 1, \dots, 6, \beta = 1, \dots, 6$) is considered to have cubic symmetry for both phases. The elastic stiffness tensor components are function of temperature. For the γ phase, the non-zero components of the stiffness tensor can be obtained as [22]: $\mathbf{C}_{11} = \mathbf{C}_{22} = \mathbf{C}_{33} = (298 - 0.096\theta)$ GPa, $\mathbf{C}_{44} = \mathbf{C}_{55} = \mathbf{C}_{66} = (139 - 0.035\theta)$ GPa, $\mathbf{C}_{12} = \mathbf{C}_{13} = \mathbf{C}_{23} = (191 - 0.057\theta)$ GPa. For the γ' phase, the non-zero components of the stiffness tensor are: $\mathbf{C}_{11} = \mathbf{C}_{22} = \mathbf{C}_{33} = (325 - 0.096\theta)$ GPa, $\mathbf{C}_{44} = \mathbf{C}_{55} = \mathbf{C}_{66} = (144 - 0.035\theta)$ GPa, $\mathbf{C}_{12} = \mathbf{C}_{13} = \mathbf{C}_{23} = (209 - 0.057\theta)$ GPa. The rest of the material constants in the constitutive model are calibrated from experiments on single crystal CMSX-4 in Ref. [11]. The alloy contains 70% volume fraction of predominantly cuboidal γ' precipitates of average size $0.45 \mu\text{m}$. The average size of the RVE selected for these tests is $0.5 \mu\text{m}$. In order to do the calibration process, a single crystal is modeled with the crystal plasticity constitutive relations for different loads. The results including Stress-strain plots from these simulations are compared with those in experiments in order to calibrate material constants. The calibrated parameters are listed in Table 1.

2.4. Validation of the sub-grain CPFEM model

The results of the crystal plasticity constitutive model for

dislocation nucleation in both γ - γ' phases stated in Section 2 in the CPFEM framework are compared to experimental data, which were performed in Refs. [23–26]. These experiments are done on CMSX-4 nickel superalloys or on a very similar compound therefore the RVE is constructed for cubic precipitates with the size of $0.45 \mu\text{m}$ located at eight corners with a 70% precipitate volume fraction. The RVE is a cube with length of $0.5 \mu\text{m}$ that is discretized into 2200, 8-noded trilinear brick elements. Minimum boundary conditions are applied as explained in Ref. [6]. The model can be used effectively to predict the mechanical behaviors of Nickel-based superalloys considering the effect of temperature from room temperature to $950 \text{ }^\circ\text{C}$, all orientations of the standard unit triangle, different quasi-static range strain rates for both tension and compression. Therefore, different creep and constant strain rate tests are performed to show the strength of the model.

Tensile constant strain tests are simulated for two orientations [001] and [111] for three temperatures $25 \text{ }^\circ\text{C}$ [25], $800 \text{ }^\circ\text{C}$ [23] and $950 \text{ }^\circ\text{C}$ [26] shown in Fig. 4(a). The simulation in room temperature is done for [111] orientation and shows high yield stress because cube slip systems are not activated in this temperature. Furthermore, the transition from the elastic to plastic part is very sharp which shows that dislocation activities in channel and matrix start almost simultaneously. Two simulations under elevated temperature are done for [001] orientation. In both simulations, it can be observed that initially plastic deformation start in channel where the slope of the elastic part changes slightly for the stress around 600 MPa. The yield stress and hardening decrease dramatically from $800 \text{ }^\circ\text{C}$ to $950 \text{ }^\circ\text{C}$. Comparison shows satisfactory agreement between the simulations and experimental data.

The second set of simulations is creep tests performed for two orientations with different intensities. As expected crystal orientation [256] is the weaker orientation and according to [24] it fails after a short time, while orientation [001] for the same creep load shows less than 1% plastic strain at the same time as shown in Fig. 4(b). According to [24] orientation [001] even doesn't fail for a long time under 820 MPa creep load and shows plastic strain around 5% after 150000s. While the creep test for a compression load for intensity of -600 MPa shows plastic strain, where simulation for tension test under the same load didn't show any plastic deformation. Comparison shows acceptable agreement between the simulations and experimental data.

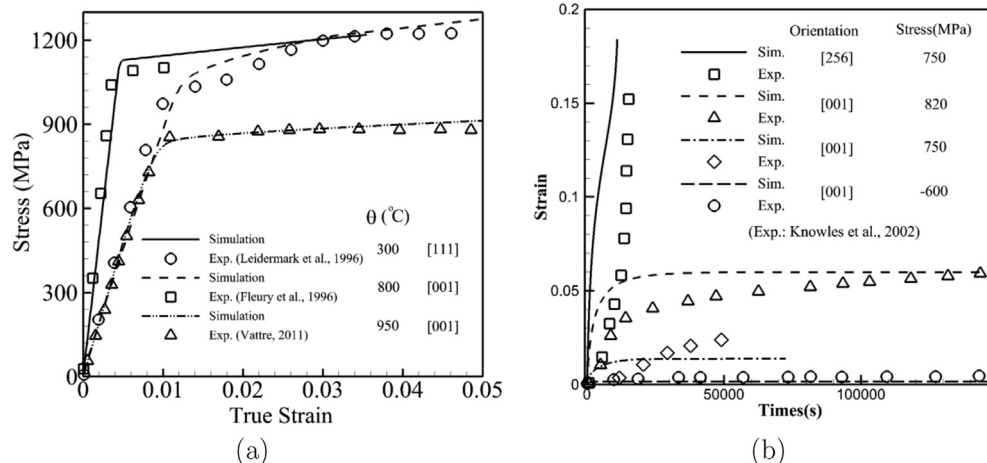


Fig. 4. Dislocation density CPFEM simulation results on Nickel-based superalloys: (a) results from the crystal plasticity sub-grain single crystal model and experiments [23,25,26] under constant strain rate 10^{-3} s^{-1} , (b) creep simulations and experiments [24] under creep tests.

3. Grain-scale crystal plasticity framework

The homogenized single crystal grain-scale for FCC Nickel superalloys is obtained from parametrized representation of the morphology of the precipitates, which is explained in Ref. [6]. The homogenized parametric constitutive model, which is a function of the morphology of the microstructure includes shape, size and volume fraction. The constitutive model is an Orowan-based model including hardening parameters, cutting (τ_{cut}^α) and passing (τ_{pass}^α) stresses that resemble thermal (s_d^α) and athermal (s_*^α) shear resistances and can be stated as:

$$\dot{\gamma}^\alpha = \begin{cases} 0 & \text{for } \tau_{eff}^\alpha \leq 0 \\ \dot{\gamma}_*^\alpha \exp \left\{ -\frac{Q}{K_B \theta} \left[1 - \left(\frac{|\tau_{eff}^\alpha|}{\tau_{cut}^\alpha} \right)^p \right]^q \right\} \text{sign}(\tau^\alpha) & \text{for } 0 < \tau_{eff}^\alpha \leq \tau_{cut}^\alpha \end{cases} \quad (13)$$

In order to incorporate the cross-slip mechanism in this length scale, cross-slip shear resistance is considered as the second mechanism contributing in the cutting stress represented in Eq. (13). The locked cross-slipped dislocations increase the hardening by acting similar to obstacles. The enthalpy term for cross-slip mechanism is extended in the same approach employed in the sub-grain scale presented in Eqs. (8)–(12). The non-Schmid components τ_{pe}^α , τ_{se}^α and τ_{cb}^α are considered to have the same duties in the sub-grain scale but in a homogenized form. Hence, the cross-slip shear resistance as a portion of cutting stress can be stated as:

$$s_{cross}^\alpha = \begin{cases} \tau_{crossco}^\alpha = \tau_{crossco}^\alpha (\tau_{pe}^\alpha, \tau_{se}^\alpha, \tau_{cb}^\alpha, \theta, \Gamma_{111}, \Gamma_{010}) & \text{on octahedral slip systems} \\ \tau_{crosscc}^\alpha = \tau_{crosscc}^\alpha (\theta) & \text{on cube slip systems} \end{cases} \quad (14)$$

The total thermal shear resistance or cutting stress can be calculated as:

$$\tau_{cut}^\alpha = s_*^\alpha + s_{cross}^\alpha \quad (15)$$

3.1. Calibrating the constitutive parameters of the single crystal grain scale

Eq. (13) holds several material constants, some are dependent to the morphology and some are not. The independent ones or fixed material constants are taken from (5). Other materials parameters, including temperature effects and the enthalpy term in Eq. (14), are calibrated by the same approach explained for the sub-grain scale using similar equations. They are listed in Table 2.

4. Homogenized AE-CP model from Sub-grain RVE model

The morphology-dependent constitutive parameters in Eq. (13) for the homogenized single crystal grain-scale model is considered to be governed by macro-micro energy equivalence [27,28], where the micromechanical analysis is conducted with the sub-grain RVE model. The constitutive model includes functional parameters in terms of morphological variables.

4.1. Morphological variables in the sub-grain microstructural RVE

The sub-grain microstructural RVE consists of two-phase γ - γ' which is characterized as three morphology variables to incorporate the volume fraction, shape and size of the γ' phase. They will be used as (1) $v_p = \frac{V_{\gamma'}}{V_{RVE}}$ for volume fraction of the γ' phase (2) n for the shape factor of the γ' phase which is obtained by considering γ' as a super-ellipsoid with the same dimension in principle directions $a = b = c$ in the equation $\left(\frac{x}{a}\right)^n + \left(\frac{y}{b}\right)^n + \left(\frac{z}{c}\right)^n = 1$, (3) l_c the distance between precipitates. Therefore, different morphology with different volume fraction, shape from spherical precipitates ($n = 2$) to cubic ones ($n \rightarrow \infty$) and different size of precipitates can be produced. For shape factor, $n_1 = \tan^{-1}(n)$ will be used instead of n for avoiding to use singular values for cubic precipitates.

4.2. Functional forms of the single crystal homogenized constitutive parameters

Four constitutive parameters in the single crystal grain scale, $s_{*0}^\alpha(n_1, v_p, l_c)$, $k(n_1, v_p, l_c)$, $k(n_1, v_p, l_p)$, $s_{sat}^\alpha(n_1, v_p, l_c)$ and $s_{cross}^\alpha(n_1, v_p, l_c)$ are calibrated by comparing the stress-strain response from the AE-CP model, with the volume-averaged response from the sub-grain RVE model simulations for constant strain-rate tests of 10^{-4} s^{-1} in the [010] direction at 800 °C. The calibration process is performed by creating 37 different RVE microstructures with different morphology including different shape factor (n), volume fraction (v_p) and channel width (l_c). In the next stage, dislocation density-based in the sub-grain scale is applied to each of these microstructures to generate a volumetric stress-strain curve up to 10% true strain. In order to satisfy Hill-Mandel principle, the same volumetric stress-strain response is generated in grain scale single crystal using AE-CP model by changing following constitutive parameters. This extensive set of simulations result the following functional forms of the single crystal constitutive parameters by using least square minimization method. The final form of these four constitutive parameters are:

Table 2
Calibrated material constants for the single crystal grain-scale model.

Parameter	k_1	k_2	ξ_0	A	θ_c	$Q(J)$	p	q	$\dot{\gamma}(s^{-1})$	$h_0(\text{MPa})$	r
Value	0.4	0.6	8	325	1600	6.5×10^{-19}	0.78	1.15	5×10^7	100	1.115

$$\begin{aligned}
 s_{s0}^\alpha(n_1, v_p, l_c) &= a_1(n_1, v_p) + \frac{b_1(n_1, v_p)}{\sqrt{l_c}} = -50v_p n_1 + 222v_p - 34n_1 + 384 + \frac{-33.3v_p n_1 + 32.92v_p + 19.61n_1 - 0.037}{\sqrt{l_c}} \\
 s_{sat}^\alpha(n_1, v_p, l_c) &= a_2(n_1, v_p) + \frac{b_2(n_1, v_p)}{l_c} = 6680v_p n_1 - 8905v_p - 1648n_1 + 3185 + \frac{-3359v_p n_1 + 5008v_p + 3631n_1 - 0.21}{\sqrt{l_c}} \\
 k_*(n_1, v_p, l_c) &= 19847v_p n_1 l_c + 12768v_p n_1 - 23120v_p l_c + 4080n_1 l_c - 7500v_p + 33n_1 - 2700l_c + 65 \\
 k(n_1, v_p, l_c) &= a_3(n_1, v_p) + \frac{b_3(n_1, v_p)}{\sqrt{l_c}} = 221.4v_p n_1 - 327.6v_p + 31.5n_1 + 5.5 + \frac{-176.5v_p n_1 + 281.2v_p - 2.44n_1 + 0.14}{\sqrt{l_c}} \\
 s_{cross}^\alpha(n_1, v_p, l_c) &= s_{cross}^\alpha * s_0(n_1, v_p, l_c), \quad s_0(n_1, v_p, l_c) = a_1(n_1, v_p) + \frac{b_1(n_1, v_p)}{\sqrt{l_c}} \\
 &= -50.32v_p n_1 + 0.538v_p - 0.09528n_1 + 1 + \frac{-0.08662v_p n_1 + 0.08566v_p + 0.051n_1 - 0.000096}{\sqrt{l_c}}
 \end{aligned} \tag{16}$$

The size dependent variable l_c reflects explicitly the size-effect due to the presence of geometrically necessary dislocations in the sub-grain scale model. The units of l_c and initial thermal resistance saturation shear resistance and cross-slip shear resistance are μm and MPa respectively, while s_0 is dimensionless.

4.3. Validation of the homogenized single crystal grain-scale model

The homogenized single crystal grain-scale model with parametric constitutive relations are validated against results from sub-grain scale and experimental data. To compare the results of this scale with the sub-grain scale, an explicit representation of the two-phase γ - γ' microstructure is constructed and the dislocation density-based model is applied for the simulation and compared with the homogenized field of the grain-scale microstructure with the parametric constitutive model. The second set is considered to compare the grain-scale model with results obtained directly from experiments for single crystal of CMSX-4 with $v_p = 70\%$ of volume fraction of in the shape of cube as γ' precipitates ($n \rightarrow \infty$). The average length of this cube is $0.45 \mu\text{m}$ and the average distance between precipitates is $0.05 \mu\text{m}$ which results in channel width $l_c = 0.0866 \mu\text{m}$. To show the ability of the proposed morphology-dependent constitutive model at the single crystal scale, three sets of simulations are conducted to investigate the effects of

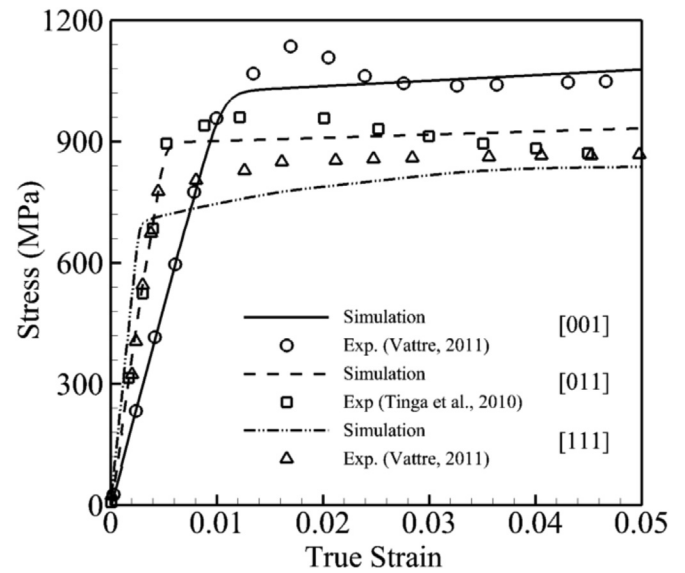


Fig. 6. Results from the crystal plasticity homogenized single crystal model and experiments [22,26] on CMSX-4 for different orientation at 850 °C under tensile strain rate of 0.001 s^{-1} .

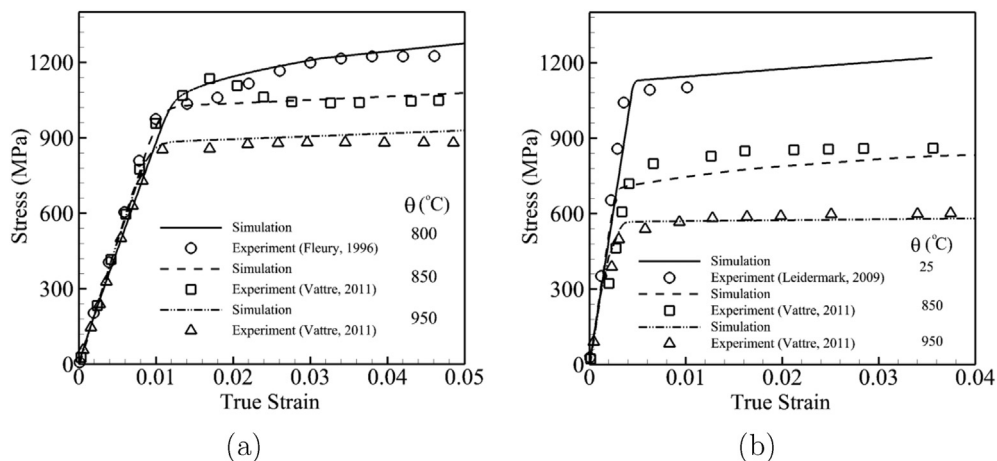


Fig. 5. Results from the crystal plasticity homogenized single crystal model and experiments [23,25,26] on CMSX-4 for different temperatures: (a) [001] orientation under tensile constant strain rate of 10^{-3} s^{-1} (b) [111] orientation under tensile constant strain rate of 10^{-4} s^{-1} .

temperature, strain-rate, orientation dependency and asymmetry in tension-compression and relaxation behavior of this material. The results of each set are compared to experimental data.

4.3.1. Effect of temperature in CMSX-4

In order to show the dependency of the model on temperature, two sets of simulations are performed. For these two sets, simulations are performed for four temperatures including room temperature, 800 °C, 850 °C and 950 °C. These two sets of simulations are done with respect to two [001] and [111] orientations at different temperature. For orientation close to [001], three constant strain rate simulations, for which experiments are performed at 800 °C [23], 850 °C [26] and 950 °C [26]. The tensile constant strain rate is 10^{-3} s^{-1} . Results from the crystal plasticity homogenized single crystal model and experiments are compared and shown in Fig. 5(a), which shows good agreement with experimental data. It can be observed that the flow stress and hardening drop as temperature increases. The second set of comparisons is done for an orientation close to [111], where three constant strain rate simulations are performed at 25 °C [25], 850 °C [26] and 950 °C [26]. The constant tensile strain rate is 10^{-4} s^{-1} . Results from the crystal plasticity homogenized single crystal model and experiments are compared and shown in Fig. 5(b) which shows quiet good agreement with experimental data. The flow stress at higher temperatures is much less than at room temperature due to activation of cube slip systems.

4.3.2. Effect of orientation and asymmetry in tension-compression in CMSX-4

Experiments on Nickel-based superalloys demonstrate significant variations with respect to orientation on the standard unit triangle, however the behavior changes as temperature increases. At temperature, with low cross-slip probability, yield stress in Nickel-based superalloys agrees with Schmid law due to same critical shear stress resistance in different orientations. No asymmetry in tension-compression is reported except for orientation close to [011]. Hence, the lowest Schmid factor results in highest yield stress. In other word, orientations close to [111] corner have the largest yield stress. The situation changes as temperature increases due to the higher probability of cross-slip and activation of cube slip systems. This is the case for temperatures higher than 1000 K where orientations close to [111] will have the smallest yield stress due to activation of cube slip systems, and significant changes will occur in critical shear stress resistance due to locking cross-slipped screw dislocations. In general for this temperature

range, orientations close to [001] show the largest yield stress in tension. The tension yield stress diminishes when approaching the [011] corner and becomes minimum for orientations close to [111] corner. However this is not the case for yield stress in compression. Orientations close to [011] corner show the largest yield stress, which reduces by approaching the [001] corner. The yield stress in compression for orientations close to [111] show minor changes with the tension tests and corresponds to the smallest yield stress. Substantial asymmetry is observed for orientations close to [001] and [011] corners on the contrary to [111] corner. In order to show orientation dependency of the model, three simulations for orientations close to three corners are performed and shown in Fig. 6. These simulations are constant strain tests with 0.001 s^{-1} tensile rate at 850 °C. The results show different yield stress and hardening behavior for these three orientations where [001] is the strongest and [111] is the weakest orientation at this temperature.

4.3.3. Relaxation behavior in CMSX-4

In order to investigate the relaxation behavior in this material, relaxation tests are performed at 850 °C for two [001] and [111] orientations and at 950 °C for [001] orientation. The constant strain rate loading at $3 \times 10^{-5} \text{ s}^{-1}$ was interrupted by 10 h relaxation segments as performed in Ref. [26]. The resulting stress relaxations are shown in Fig. 7.

5. Conclusions

This paper develops non-Schmid constitutive models for two scales and bridges these scales in a hierarchical framework from two-phase γ - γ' sub-grain scale to a homogenized single crystal grain-scale constitutive model. For the single crystal or grain scale, a homogenized crystal plasticity finite element model is developed, which includes both non-Schmid effects and morphology variables of precipitates. Cross-slip mechanism is included in the enthalpy term, which is a function of the anti-phase boundary energies and the non-Schmid shear stresses. The non-Schmid components τ_{pe}^{α} , τ_{se}^{α} and τ_{cb}^{α} are the main factor in the dislocation dissociation and they are slip system dependent. The hardening parameters in the sub-grain γ - γ' include statistically stored dislocations, cross-slip dislocations and geometrically necessary dislocations. The homogenized model incorporates the sub-grain γ - γ' morphology, viz. the size, shape and volume fraction of the γ' particles. The constitutive model in the homogenized grain scale includes the thermal shear resistance, the saturation shear resistance, the reference slip-rate and cross-slip shear resistance as four

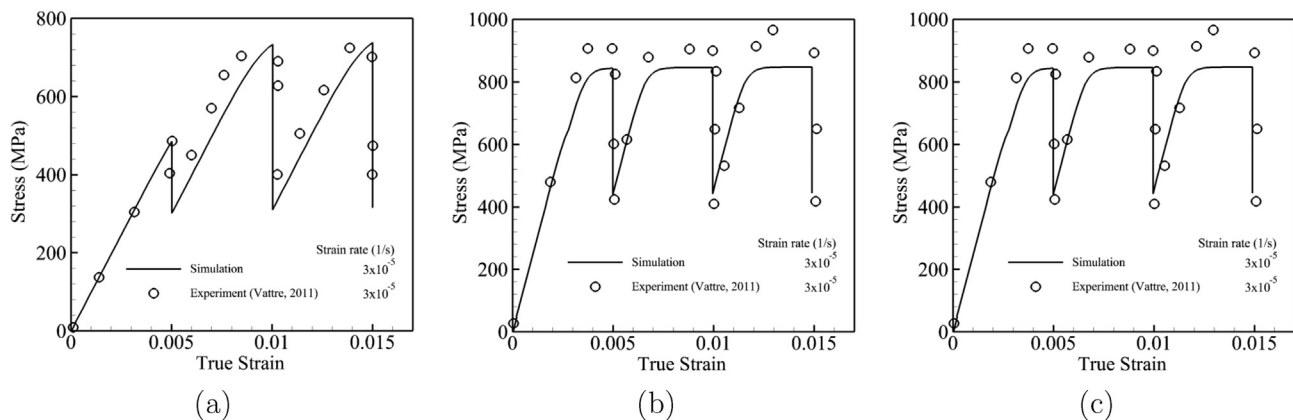


Fig. 7. Results from the crystal plasticity homogenized single crystal model and experiments [26] on CMSX-4 under different relaxation strain rate: (a) [001] orientation at 850 °C (b) [001] orientation at 950 °C (c) [111] orientation at 850 °C.

homogenized parameters, which are given as functions of the γ' morphology. There is a size dependency in the two-scale model where it naturally occurs in the sub-grain scale due to the presence of gradient of plastic deformation especially near interface of two phases, and is passed in the homogenized single crystal grain scale model through the channel-width. Not only can the homogenized activation energy-based crystal plasticity model reproduce the results of the sub-grain scale but the results from this model are in good agreement with the experimental results. Tension-compression asymmetry and orientation dependency of these alloys, observed in experiments, are well represented by this model. The overall hierarchical model has the potential of significantly expediting polycrystalline simulations, while retaining accuracy.

Acknowledgments

Shahriyar Keshavarz acknowledges support from the U.S. Department of Commerce, National Institute of Standards and Technology under financial assistance award 70NANB15H240. Somnath Ghosh has been supported through a grant No. FA9550-12-1-0445 to the Center of Excellence on Integrated Materials Modeling (CEIMM) at Johns Hopkins University awarded by the AFOSR/RSL Computational Mathematics Program (Manager Dr. A. Sayir) and AFRL/RX (Monitors Dr. C. Woodward and C. Przybyla). This sponsorship is gratefully acknowledged.

References

- [1] V. Paidar, V. Vitek, Stacking fault-type interfaces and their role in deformation, in: *Intermetallic Compounds, Progress*, Vol. 3, John Wiley Chichester, 2002, p. 437.
- [2] R. Unocic, L. Kovarik, C. Shen, P. Sarosi, Y. Wang, J. Li, S. Ghosh, M. Mills, Deformation mechanisms in ni-base disk superalloys at higher temperatures, *Superalloys 8* (2008) 377.
- [3] T.M. Pollock, S. Tin, Nickel-based superalloys for advanced turbine engines: chemistry, microstructure and properties, *J. Propuls. Power* 22 (2) (2006) 361–374.
- [4] S. Ghosh, S. Keshavarz, G. Weber, Computational multiscale modeling of nickel-based superalloys containing gamma-gamma' precipitates, in: *Inelastic Behavior of Materials and Structures Under Monotonic and Cyclic Loading*, Springer, 2015, pp. 67–96.
- [5] M. Ignat, J.-Y. Buffiere, J. Chaix, Microstructures induced by a stress gradient in a nickel-based superalloy, *Acta Metallurgica Materialia* 41 (3) (1993) 855–862.
- [6] S. Keshavarz, S. Ghosh, Multi-scale crystal plasticity finite element model approach to modeling nickel-based superalloys, *Acta Mater.* 61 (17) (2013) 6549–6561.
- [7] R.R. Unocic, N. Zhou, L. Kovarik, C. Shen, Y. Wang, M.J. Mills, Dislocation decorrelation and relationship to deformation microtwins during creep of a γ precipitate strengthened ni-based superalloy, *Acta Mater.* 59 (19) (2011) 7325–7339.
- [8] J. Cormier, X. Milhet, J. Mendez, Non-isothermal creep at very high temperature of the nickel-based single crystal superalloy mc2, *Acta Mater.* 55 (18) (2007) 6250–6259.
- [9] P. Lours, A. Coujou, P. Coulomb, On the deformation of the; 100_i orientated γ strengthening phase of the cmsx2 superalloy, *Acta Metallurgica Materialia* 39 (8) (1991) 1787–1797.
- [10] V. Paidar, D. Pope, V. Vitek, A theory of the anomalous yield behavior in 11 2 ordered alloys, *Acta Metall.* 32 (3) (1984) 435–448.
- [11] C. Allan, Plasticity of Nickel Base Single Crystal Superalloys, Ph.D. thesis, Massachusetts Institute of Technology, 1995.
- [12] S. Keshavarz, S. Ghosh, Hierarchical crystal plasticity fe model for nickel-based superalloys: sub-grain microstructures to polycrystalline aggregates, *Int. J. Solids Struct.* 55 (2015) 17–31.
- [13] S. Ghosh, S. Keshavarz, Multi-scale crystal plasticity fem approach to modeling nickel- based superalloys, in: 55th AIAA/ASME/ASCE/AHS/SC Structures, Structural Dynamics, and Materials Conference, 2014, p. 0796.
- [14] S. Groh, E. Marin, M. Horstemeyer, H. Zbib, Multiscale modeling of the plasticity in an aluminum single crystal, *Int. J. Plasticity* 25 (8) (2009) 1456–1473.
- [15] M.G. Moghaddam, A. Achuthan, B. Bednarczyk, S. Arnold, E. Pineda, A multi-scale computational model using generalized method of cells (gmc) homogenization for multi-phase single crystal metals., *Comput. Mater. Sci.* 96 (2015) 44–55.
- [16] S. Ghosh, G. Weber, S. Keshavarz, Multiscale modeling of polycrystalline nickel-based superalloys accounting for subgrain microstructures, *Mech. Res. Commun.*
- [17] A.C. Reid, S.A. Langer, R.C. Lua, V.R. Coffman, S.-I. Haan, E. García, Image-based finite element mesh construction for material microstructures, *Comput. Mater. Sci.* 43 (2008) 989–999.
- [18] S. Keshavarz, S. Ghosh, A crystal plasticity finite element model for flow stress anomalies in ni3Al single crystals, *Philos. Mag.* 95 (24) (2015) 2639–2660.
- [19] E. Schmid, W. Boas, *Plasticity of Crystals*, Citeseer, 1950.
- [20] F. Roters, P. Eisenlohr, L. Hantcherli, D. Tjahjanto, T. Bieler, D. Raabe, Overview of constitutive laws, kinematics, homogenization and multiscale methods in crystal plasticity finite-element modeling: theory, experiments, applications, *Acta Mater.* 58 (4) (2010) 1152–1211.
- [21] A.M. Cuitino, M. Ortiz, Computational modelling of single crystals, *Model. Simul. Mater. Sci. Eng.* 1 (3) (1993) 225.
- [22] T. Tinga, W. Brekelmans, M. Geers, Time-incremental creep–fatigue damage rule for single crystal ni-base superalloys, *Mater. Sci. Eng. A* 508 (1) (2009) 200–208.
- [23] G. Fleury, F. Schubert, H. Nickel, Modelling of the thermo-mechanical behaviour of the single crystal superalloy cmsx-4, *Comput. Mater. Sci.* 7 (1) (1996) 187–193.
- [24] D. Knowles, S. Gunturi, The role of; 112_i{ 111} slip in the asymmetric nature of creep of single crystal superalloy cmsx-4, *Mater. Sci. Eng. A* 328 (1) (2002) 223–237.
- [25] D. Leidermark, J.J. Moverare, K. Simonsson, S. Sjöström, S. Johansson, Room temperature yield behaviour of a single-crystal nickel-base superalloy with tension/compression asymmetry, *Comput. Mater. Sci.* 47 (2) (2009) 366–372.
- [26] A. Vattré, B. Fedelich, On the relationship between anisotropic yield strength and internal stresses in single crystal superalloys, *Mech. Mater.* 43 (12) (2011) 930–951.
- [27] R. Hill, On macroscopic effects of heterogeneity in elastoplastic media at finite strain, in: *Mathematical Proceedings of the Cambridge Philosophical Society*, Vol. 95, Cambridge Univ Press, 1984, pp. 481–494.
- [28] S. Nemat-Nasser, Averaging theorems in finite deformation plasticity, *Mech. Mater.* 31 (8) (1999) 493–523.